

---

# **ELECTRODEPOSITION OF METAL MATRIX COMPOSITES AND MATERIALS CHARACTERIZATION FOR THIN-FILM SOLAR CELLS**

**Sang M. Han**

**University of New Mexico  
1700 Lomas Blvd. NE, Suite 2200  
Albuquerque, NM 87131-0001**

**4 Dec 2017**

**Final Report**

**APPROVED FOR PUBLIC RELEASE; DISTRIBUTION IS UNLIMITED.**



**AIR FORCE RESEARCH LABORATORY  
Space Vehicles Directorate  
3550 Aberdeen Ave SE  
AIR FORCE MATERIEL COMMAND  
KIRTLAND AIR FORCE BASE, NM 87117-5776**

---

**DTIC COPY**  
**NOTICE AND SIGNATURE PAGE**

Using Government drawings, specifications, or other data included in this document for any purpose other than Government procurement does not in any way obligate the U.S. Government. The fact that the Government formulated or supplied the drawings, specifications, or other data does not license the holder or any other person or corporation; or convey any rights or permission to manufacture, use, or sell any patented invention that may relate to them.

This report is the result of contracted fundamental research which is exempt from public affairs security and policy review in accordance with AFI 61-201, paragraph 2.3.5.1. This report is available to the general public, including foreign nationals. Copies may be obtained from the Defense Technical Information Center (DTIC) (<http://www.dtic.mil>).

**AFRL-RV-PS-TR-2017-0174 HAS BEEN REVIEWED AND IS APPROVED FOR  
PUBLICATION IN ACCORDANCE WITH ASSIGNED DISTRIBUTION STATEMENT.**

//SIGNED//  
DAVID WILT  
Program Manager

//SIGNED//  
PAUL HAUSGEN, Ph.D.  
Technical Advisor, Spacecraft Component Technology

//SIGNED//  
JOHN BEAUCHEMIN  
Chief Engineer, Spacecraft Technology Division  
Space Vehicles Directorate

This report is published in the interest of scientific and technical information exchange, and its publication does not constitute the Government's approval or disapproval of its ideas or findings.

Approved for public release; distribution is unlimited.

# REPORT DOCUMENTATION PAGE

Form Approved  
OMB No. 0704-0188

Public reporting burden for this collection of information is estimated to average 1 hour per response, including the time for reviewing instructions, searching existing data sources, gathering and maintaining the data needed, and completing and reviewing this collection of information. Send comments regarding this burden estimate or any other aspect of this collection of information, including suggestions for reducing this burden to Department of Defense, Washington Headquarters Services, Directorate for Information Operations and Reports (0704-0188), 1215 Jefferson Davis Highway, Suite 1204, Arlington, VA 22202-4302. Respondents should be aware that notwithstanding any other provision of law, no person shall be subject to any penalty for failing to comply with a collection of information if it does not display a currently valid OMB control number. PLEASE DO NOT RETURN YOUR FORM TO THE ABOVE ADDRESS.

1. REPORT DATE (DD-MM-YYYY) 04-12-2017	2. REPORT TYPE Final Report	3. DATES COVERED (From - To) 04 Aug 2014 - 04 Nov 2017		
4. TITLE AND SUBTITLE  Electrodeposition of Metal Matrix Composites and Materials Characterization for Thin-Film Solar Cells		5a. CONTRACT NUMBER FA9453-14-1-0242		
		5b. GRANT NUMBER		
		5c. PROGRAM ELEMENT NUMBER 62601F		
6. AUTHOR(S)  Sang M. Han		5d. PROJECT NUMBER 8809		
		5e. TASK NUMBER PPM00015925		
		5f. WORK UNIT NUMBER EF124941		
7. PERFORMING ORGANIZATION NAME(S) AND ADDRESS(ES)  University of New Mexico 1700 Lomas Blvd. NE, Suite 2200 Albuquerque, NM 87131-0001		8. PERFORMING ORGANIZATION REPORT NUMBER		
9. SPONSORING / MONITORING AGENCY NAME(S) AND ADDRESS(ES)  Air Force Research Laboratory Space Vehicles Directorate 3550 Aberdeen Ave SE Kirtland AFB, NM 87117-5776		10. SPONSOR/MONITOR'S ACRONYM(S) AFRL/RVSV		
		11. SPONSOR/MONITOR'S REPORT NUMBER(S) AFRL-RV-PS-TR-2017-0174		
12. DISTRIBUTION / AVAILABILITY STATEMENT Approved for public release; distribution is unlimited.				
13. SUPPLEMENTARY NOTES				
14. ABSTRACT We have demonstrated that metal matrix composites, which consist of silver-multiwalled carbon nanotube-silver, layer-by-layer stack, can electrically bridge the cracks (>40 $\mu$ m) that appear in the semiconductor substrates and the composite grid lines. This gap bridging was proven to be repeatable through strained-to-failure/closed-gap repeat cycles. For device demonstration, the composites were integrated onto commercial triple-junction cells, and the composite-enhanced cells showed strong crack-tolerance, maintaining >95% of the short circuit current upon substrate fracture. By contrast, the conventional metallization led to >50% loss in short circuit current. The composite metallization was also superior in minimizing the overall efficiency loss against fracture, compared to the conventional metallization. During the project extension period, we have initiated composite materials modeling and circuit modeling to establish microstructure-mechanical/electrical property relationship.				
15. SUBJECT TERMS metal matrix composite, carbon nanotube reinforced silver, reinforced photovoltaic				
16. SECURITY CLASSIFICATION OF:  a. REPORT Unclassified		17. LIMITATION OF ABSTRACT Unlimited	18. NUMBER OF PAGES 30	19a. NAME OF RESPONSIBLE PERSON David Wilt
b. ABSTRACT Unclassified				19b. TELEPHONE NUMBER (include area code)
c. THIS PAGE Unclassified				

--- This Page Intentionally Left Blank ---

## TABLE OF CONTENTS

<b>1</b>	<b>Summary.....</b>	<b>1</b>
<b>2</b>	<b>Introduction.....</b>	<b>2</b>
<b>3</b>	<b>Methods, Assumptions, and Procedures .....</b>	<b>4</b>
<b>3.1</b>	<b>Metal Matrix Composites.....</b>	<b>4</b>
3.1.1	Choice of Composite Deposition Method.....	4
3.1.2.	Carbon Nanotube Surface Functionalization and Microstructure .....	5
<b>3.2</b>	<b>Composite Characterization .....</b>	<b>6</b>
<b>3.3</b>	<b>Cell Integration and Performance Characterization.....</b>	<b>8</b>
<b>4</b>	<b>Results and discussion .....</b>	<b>9</b>
<b>4.1</b>	<b>Cell Performance Characterization and Modeling.....</b>	<b>9</b>
<b>4.2</b>	<b>Circuit Modeling to Extract Cell Parameters .....</b>	<b>10</b>
<b>4.3</b>	<b>Composite Modeling to Predict Mechanical Properties .....</b>	<b>13</b>
<b>5</b>	<b>Conclusions.....</b>	<b>16</b>
	<b>References.....</b>	<b>17</b>
	<b>List of Acronyms, Abbreviations, and Symbols .....</b>	<b>21</b>

Approved for public release; distribution is unlimited.

## LIST OF FIGURES

Figure 1: Cell fracture and power loss.....	1
Figure 2: Schematic architecture of IMM cell.....	2
Figure 3: SEM micrographs of CNTs bridging gaps.....	2
Figure 4: Conceptual diagram of toughening mechanisms.....	4
Figure 5: Controlling CNT solubility in water.....	5
Figure 6: Schematic diagram of two main MMC microstructures. ....	6
Figure 7: RACK electromechanical testing setup.....	7
Figure 8: Process flow for MMC integration onto commercial TJ cells. ....	8
Figure 9: LIV and EL measurements on control sample (left) with 100% Ag gridlines, and test sample (right) with MMC gridlines. ....	9
Figure 10: SPICE modeling of cracked TJ cells and their simulated IV curves with varying series resistance.....	10
Figure 11: <i>DIV</i> curves of SolAero’s ZTJ triple-junction PV cells reinforced with MMCs before and after the substrate fracture.....	11
Figure 12: <i>LIV</i> curves of SolAero’s ZTJ triple-junction PV cells reinforced with MMCs before and after the substrate fracture.....	12
Figure 13: MMC composite microstructure modeled by a layer-by-layer construct of Ag/CNT/Ag stack. ....	14
Figure 14: Experimental and model stress-strain curves of Ag deposited by evaporation.....	14

## LIST OF TABLES

Table 1: Summary of advantages and disadvantages of common metal and MMC deposition techniques.....	5
Table 2: Device performance parameters extracted from model fit to experimental <i>DIV</i> and <i>LIV</i> curves.....	13
Table 3: Summary of MMC modulus as a function of CNT loading. ....	15

## **ACKNOWLEDGMENTS**

This material is based on research sponsored by Air Force Research Laboratory under agreement number FA9453-14-1-0242. The U.S. Government is authorized to reproduce and distribute reprints for Governmental purposes notwithstanding any copyright notation thereon.

## **DISCLAIMER**

The views and conclusions contained herein are those of the authors and should not be interpreted as necessarily representing the official policies or endorsements, either expressed or implied, of Air Force Research Laboratory or the U.S. Government.

This Page Intentionally Left Blank

Approved for public release; distribution is unlimited.

## 1 SUMMARY

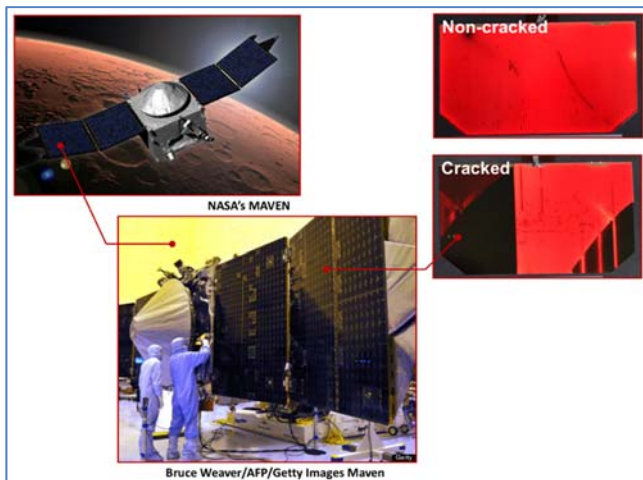


**Figure 1:** Cell fracture and power loss

Today high-efficiency, thin-film-based photovoltaic (PV) cells power space vehicles. Figure 1 shows National Aeronautics and Space Administration (NASA's) Mars Atmosphere and Volatile Evolution Mission (MAVEN) probe as an example, where these cells are mounted on solar panels that power the space vehicle. Due to the mechanical nature of thin films, however, these solar cells are susceptible to fracture (also known as micro-cracks or cracks) during manufacturing, transportation, installation, and operation, requiring costly pre-flight replacement and potentially compromising the mission lifetime. The electroluminescence images of

a commercial multijunction (MJ) cell in Figure 1 clearly illustrate how the substrate fracture can propagate through metal contacts, electrically isolating fractured regions that no longer generate power. Considering the desired mission lifetime of space vehicles (e.g., >15 years for geosynchronous earth orbit operation), the goal of this project was to develop an advanced, commercially competitive, metallization scheme for thin-film, MJ solar cells to mitigate the adverse impact of substrate and metal fractures. Our advanced metallization scheme relied on electrochemical deposition of silver and incorporation of multiwalled carbon nanotubes into the silver matrix to mitigate the negative impact of cracks.

During the entire project period of 08/04/2014 – 08/03/17, we have (1) developed stable surface chemical functionalization methods for multiwalled carbon nanotubes to make them water-soluble and to enhance their adhesion strength to surrounding metal matrix, (2) integrated metal matrix composites onto commercial triple-junction cells, (3) characterized cell performance to demonstrate that metal matrix composites can improve crack-tolerance by maintaining the short circuit current >95% and the cell efficiency loss < 19%, whereas standard metallization leads to short circuit current loss >50% and the cell efficiency loss >54%, (4) initiated composite modeling to establish microstructure-mechanical/electrical property relationship, and (5) initiated circuit modeling to extract device parameters (e.g., ideality factor) and required loading (wt%) of carbon nanotubes to maximize the cell performance despite fractures. In addition, we have an issued International Patent WO 2016/205722 A1 that originated from this research, and the technology is currently licensed to Osazda Energy, LLC.

## 2 INTRODUCTION

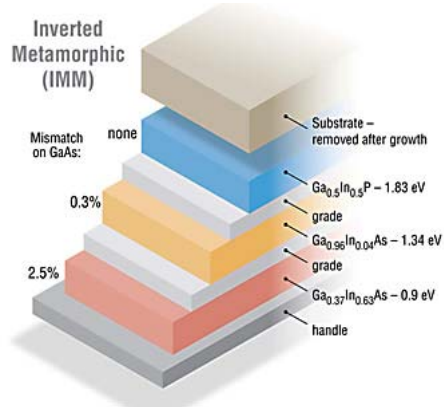


**Figure 2:** Schematic architecture of IMM cell<sup>9</sup>

The current trend in both space and terrestrial photovoltaics is to implement high-efficiency, thin-film-based solar cells to reduce weight and materials cost, while improving the performance. For space photovoltaics, MJ solar cells have been used almost exclusively due to their high efficiency<sup>1,2</sup> and high radiation hardness<sup>3</sup>. The efficiency of state-of-practice triple-junction (TJ) cells used in space today is approximately 30% under 1-sun Air Mass 0 (AM0) spectrum<sup>4,5</sup>. Multijunction technology involves stacking different bandgap subcells electrically and optically in series, connected by tunnel junctions, to effectively capture and utilize the solar spectrum<sup>2,6</sup>. State-of-practice TJ cells consist of GaInP<sub>2</sub> and (In)GaAs subcells grown lattice-matched via metal organic vapor phase epitaxy on an active Ge substrate<sup>1,7-9</sup>. In recent years, for

improved performance over the state-of-practice TJ cells, other cell architectures are being explored, such as inverted metamorphic multijunction (IMM)<sup>10-13</sup> solar cells. Figure 2 shows a schematic view of IMM cell architecture<sup>14</sup>, where InGaP and InGaAs subcells are sequentially grown on a lattice-matched substrate. After completing the growth, only the stack of active layers is exfoliated and transferred to a light-weight handling substrate, where the stack is inverted, such that the InGaP layer faces the sun. This new architecture eliminates the use of Ge substrates as well as Ge bottom cell found in traditional TJ solar cells, providing better current matching, higher efficiency, and lighter weight. As the cells become thinner, however, we expect the cell fracture to be a greater concern when these thin-film cells are subjected to thermomechanical stress, such as prolonged temperature fluctuations encountered in low earth orbit operation. The mismatch in thermal expansion coefficients of semiconductor and metal is an inherent engineering problem.

To minimize the detrimental effects of severed metal busbars and gridlines on solar cell performance, we have explored incorporating multiwalled carbon nanotubes (MW-CNTs) into silver (Ag), forming a metal matrix composite (MMC).<sup>15,16</sup> We have discovered that with proper CNT surface functionalization and judiciously designed composite microstructure (see Section 4.2), the CNTs in MMC gridlines can electrically bridge gaps greater

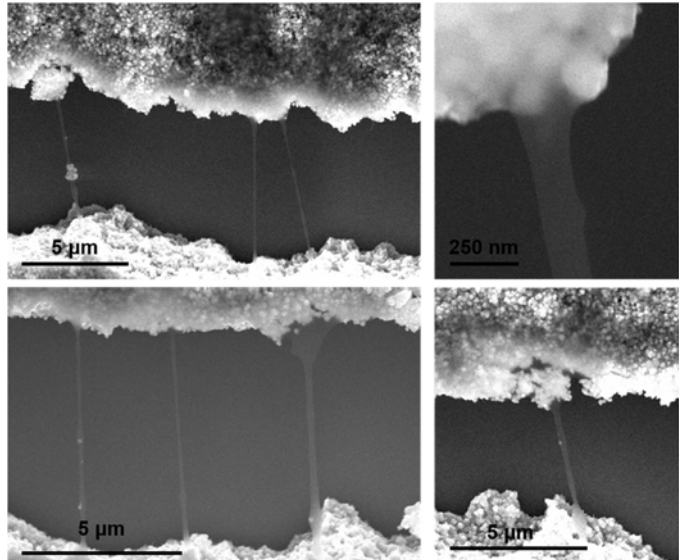


**Figure 3:** SEM micrographs of CNTs bridging gaps<sup>16</sup>

than 40  $\mu\text{m}$ .<sup>16</sup> The scanning electron micrograph (SEM) images in Figure 3 conceptually demonstrate this composite engineering strategy, where the CNTs mechanically and electrically bridge the gaps in severed MMC gridlines, providing redundant electrical conduction pathways. We note that we are showing only 9- $\mu\text{m}$ -wide gaps here because of the practical difficulty of transferring fractured samples with large gaps into the SEM vacuum chamber. In addition to gap-bridging, we have demonstrated that the MMC gridlines, which are strained to failure by greater than 40  $\mu\text{m}$  displacement, can “self-heal” to re-establish electrical conduction, when the gap is closed.<sup>16</sup> This self-healing is proven to be repeatable over many strain-to-failure/closed-gap cycles.<sup>16</sup> Most importantly, our preliminary device characterization on MMC-enhanced commercial TJ cells has shown substantially improved crack-tolerance compared to the cells with conventional evaporation-based metallization<sup>15</sup>

### 3 METHODS, ASSUMPTIONS, AND PROCEDURES

#### 3.1 Metal Matrix Composites

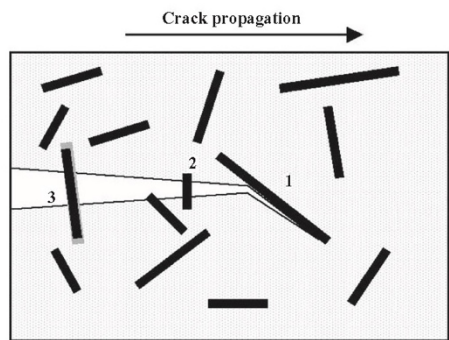


**Figure 4:** Conceptual diagram of toughening mechanisms<sup>29</sup>.

Multiwalled carbon nanotubes (MW-CNTs) possess exceptionally high elastic modulus (~TPa range)<sup>17,18</sup> and current carrying capacity ( $>10^7$  A/cm<sup>2</sup>)<sup>19-21</sup>, while being much more cost-effective (by an order of magnitude per unit weight<sup>22</sup>) than single-walled carbon nanotubes (SW-CNTs). Carbon nanotubes can be incorporated into metal<sup>23-29</sup> to enhance the composite mechanical strength<sup>23,24,30,31</sup> without significantly increasing the resistivity compared to that of the metal<sup>23</sup>. A number of different mechanisms have been postulated to explain the toughening, which is very much analogous to whisker and fiber reinforcement shown in Figure 4<sup>30</sup>: (1) crack deflection at the CNT-metal boundary, (2) crack bridging where CNTs are strongly adhered to metal and thus highly strained between two fractured metal surfaces, and (3) CNT pullout where CNTs slide out of metal matrix leaving a void behind.<sup>30</sup>

The electrical properties of MMCs largely depend on CNT-metal interface and how clustered CNTs are within the metal matrix.<sup>23</sup> Poor adhesion to metal and clustering are believed to increase the resistivity of the composite.<sup>23</sup> Thus, much effort has been made to disperse CNTs and homogeneously incorporate them into metal.<sup>23</sup> Here, we have selected MW-CNTs as our material choice for two main reasons. (1) MW-CNTs are much more cost-effective than SW-CNTs.<sup>22</sup> Even at the research-level purchasing price, the amount of CNTs we are using would add only about \$5 per m<sup>2</sup> of panel surface area. This cost can be easily offset by the savings in Ag usage, since we will be employing electroplating, rather than evaporation or screen printing. (2) MW-CNT MMCs possess superior gap-bridging capability (10s of  $\mu$ m) with “self-healing” characteristics compared to SW-CNT MMCs (a few  $\mu$ m) that irreversibly fail under large strain ( $>10$  of  $\mu$ m).

##### 3.1.1 Choice of Composite Deposition Method

Numerous techniques exist today to deposit MMCs, including powder metallurgy route, melting and solidification route, thermal spray route, and electrochemical route.<sup>23</sup> Other methods, such as screen printing<sup>24</sup> and mechanical rolling<sup>32</sup>, are also available. Here, we chose the electrochemical route because the technique is cost-competitive and high-throughput over large areas. The usage of Ag in electroplating is also minimal compared to other techniques. Screen printing is another low-cost manufacturing technique for metal deposition, widely used in the terrestrial PV market, but the resolution is limited to wide gridlines ( $> 70$   $\mu$ m), and the electrical/optical quality is not as good as electroplated metal.<sup>33</sup> Since space PV gridlines typically require finer resolution (15 to 30  $\mu$ m) and larger current density ( $\sim 50$  mA/cm<sup>2</sup>) than what is readily achievable by screen printing, electrochemical deposition became our choice for metal deposition. We have also considered metal evaporation, which is the standard approach for space PV front contacts; however, the vacuum technique is not easily amenable to CNT incorporation. The

advantages and disadvantages of a few key deposition techniques are summarized in Table 1 below for clarity.

**Table 1:** Summary of advantages and disadvantages of common metal and MMC deposition techniques

Technique	Advantages	Disadvantages
Electrochemical deposition (also known as electroplating or plating)	Low-cost, large-area, high-throughput technique. Higher electrical conductivity and finer resolution than screen printing. Less metal consumption than screen printing.	Extra lithographical step needed during processing. Potential metal contamination.
Screen printing	Low-cost and widely used in terrestrial PV market.	Less conductive than electrochemically deposited metal. Limited line resolution. Larger consumption of metal than electroplating.
Evaporation	Widely used, proven technique in space PV market.	Vacuum technique not easily amenable to simultaneous CNT incorporation or wet chemistry. Larger consumption of metal than electroplating.

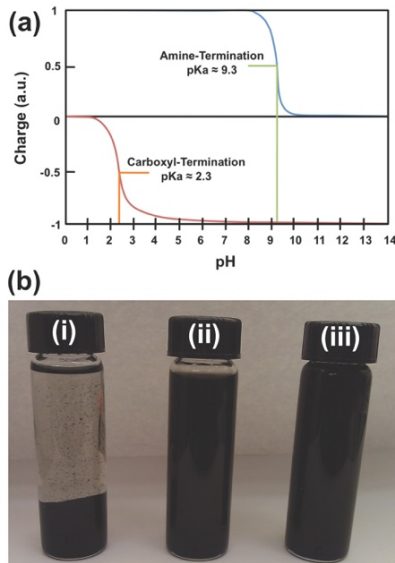


**Figure 5:** Controlling CNT solubility in water.

Protocols for surface functionalizing CNTs are available in literature<sup>34-36</sup>. For our work, we have chosen carboxylic ( $-\text{COOH}$ ) and amine ( $-\text{NH}_2$ ) terminations.  $\text{pKa}$  of carboxylic groups<sup>37</sup> can range from 0.5 to 4.2, while  $\text{pKa}$  of amine<sup>38</sup> groups can range from 9.3 to 9.8. These values suggest that at neutral  $\text{pH} = 7$ , carboxylic-terminated CNTs would be negatively charged, whereas amine-terminated CNTs would be positively charged. Figure 5(a) conceptually describes how the net surface charge on CNTs would vary as a function of surface functional group and solution  $\text{pH}$ . To demonstrate that the CNTs can be functionalized to become charged and hydrophilic, Figure 5(b-ii) shows our carboxylic-terminated CNTs completely solubilized in water. The hydrophilicity and water solubility indicate high-energy surface. Our mechanical strain failure test and tape adhesion test

on MMCs, combined with SEM inspection, have additionally indicated that organic surface functionalization increases the adhesion strength of CNTs to metal matrix.

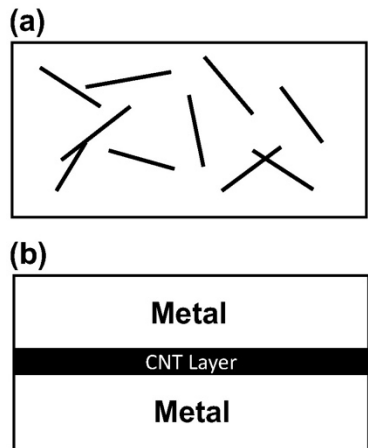


**Figure 6:** Schematic diagram of two main MMC microstructures.

Since we are depositing metal cations (e.g.,  $\text{Ag}^+$ ) on the solar cell substrate working as a negatively biased cathode, the cationic amine termination (i.e.,  $-\text{NH}_3^+$ ) can be used to co-deposit CNTs with metal. The co-deposition would create a network of homogeneously distributed CNTs embedded in metal [see Figure 6(a)]. This is the most common microstructure for CNT-metal composites. Alternatively, the positively charged CNTs can be deposited by themselves in a separate batch, following the 1<sup>st</sup> metal deposition. Then, another layer of metal can be deposited on top of the CNT layer to create a metal-CNT-metal, layer-by-layer microstructure [see Figure 6(b)]. Depending on the coverage and overlap of CNTs, the 2<sup>nd</sup> metal layer can intercalate through the CNT network and connect with the 1<sup>st</sup> metal layer. The layering can be repeated if multiple layers are desired.

In comparison, the anionic carboxylic termination (i.e.,  $-\text{COO}^-$ ) can be used to combine metal erosion (roughening of metal surface) and CNT incorporation to create a more complex microstructure, while the solar cell substrate functions as a positively biased anode. Metal deposition can ensue after the CNT deposition to bury the CNTs, creating a metal-CNT-metal, layer-by-layer microstructure with a highly corrugated interface between metal and CNT layers. Negatively charged CNTs can also be deposited on the positively biased substrate in a separate batch after metal deposition. The following 2<sup>nd</sup> metal layer deposition on CNTs would create a metal-CNT-metal, layer-by-layer structure, but with a much better defined interface between metal and CNT layers. The layering can be repeated if multiple layers are desired. The 3<sup>rd</sup> approach is where the negatively charged CNTs, well dispersed in an aqueous solution, are spray-coated on the 1<sup>st</sup> metal layer. The 2<sup>nd</sup> metal layer can then be deposited on CNTs to create a metal-CNT-metal, layer-by-layer structure. Again, the layering can be repeated if multiple layers are desired.

While the deposition approaches described above illustrate how we can manipulate the MMC microstructure in a variety of different ways, we have experimentally observed that the electrokinetic mobility of metal cations (e.g.,  $\text{Ag}^+$  and  $\text{Cu}^{2+}$ ) is vastly greater than that of charged CNTs. This disparity places a limit on the rate at which CNTs can be incorporated into metal. Therefore, in our published work<sup>15,16,39</sup>, we have focused on the metal/CNT/metal sandwiched microstructure, where the CNT layer is spray-coated to achieve high incorporation rate (i.e., fast CNT deposition), and was the primary focus of our work.

### 3.2 Composite Characterization

The CNT-Ag MMCs can be characterized for mechanical and electrical properties. The mechanical characterization may include stress-strain measurements by Dynamic Mechanical

Analysis (DMA)<sup>31,40</sup>, where a free-standing MMC composite line in a dog-bone shape<sup>32</sup> would be uniaxially strained to estimate the elastic modulus. Shear testing can also be performed, where the composite gridlines on a semiconductor substrate are mechanically scraped from the side to measure the adhesion strength as well as the mechanical strength of the gridlines. Controlled adhesion test can also be performed to quantitatively measure only the adhesion strength. For electrical characterization, one could also use a four-point probe to measure the sheet resistance (thus conductivity) of the composite gridlines. The typical conductivity of our composite gridlines is on the order of  $3.0 \times 10^5 \Omega\text{-cm}$  compared to pure silver ( $1.2 \times 10^5 \Omega\text{-cm}$ ), emphasizing the excellent electrical properties of CNTs and their good adhesion to the Ag matrix.

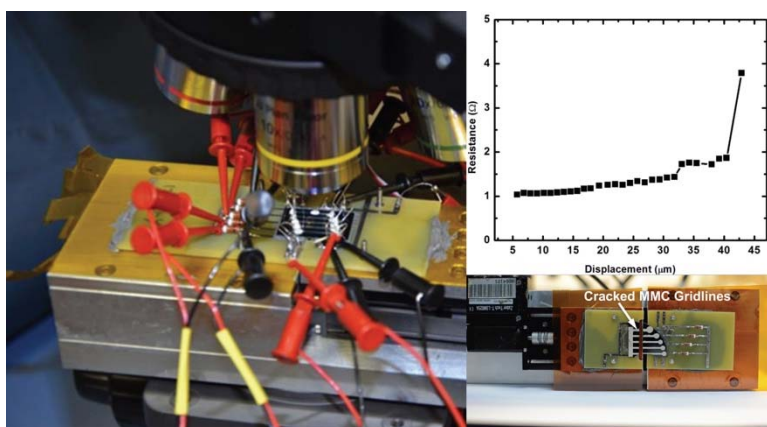


**Figure 7:** RACK electromechanical testing setup.

For simultaneous electro-mechanical characterization, we have developed Resistance Across Cleaves and cracKs (RACK) testing method, where the composite gridlines deposited on a semiconductor substrate are mechanically strained to failure to form a crack, while the electrical resistance through each gridline is measured.<sup>16</sup> The gap in the fractured metal lines is also optically measured under a microscope, as the lines are pulled apart.

Figure 7 shows the RACK testing setup. A set of parallel MMC gridlines, deposited on an InP substrate, are first mounted on two printed circuit boards using an adhesive. Upon curing the adhesive, the substrate is scribed with a diamond tip to generate a crack that propagates across the substrate backside, orthogonal in direction to the MMC gridlines. The cracked substrate is then attached to a linear stage controlled by a stepper motor. The resistance across each of the MMC gridlines is continuously recorded as the gridlines are pulled apart at micron increments until the electrical resistivity approaches infinity upon plastic failure. *Note that this electrical failure (i.e., sharply rising line resistance) does not occur until the gap in the fracture line is as much as 40  $\mu\text{m}$ .* Following the first electrical disconnect, the gap is incrementally closed in reverse until the electrical connection is reestablished across the gridlines (“self-healing”); the substrate is then pulled apart again. This process is repeated until no further change is seen in the gap width at which the electrical connection is lost and regained. *This “self-healing” characteristic is unique to our MMCs.*

*The RACK testing provides as a function of CNT loading (i.e., CNT surface coverage in the layer-by-layer structure) (1) the maximum bridgeable gap, (2) the line resistance through the CNT network upon metal line fracture and at the maximum bridgeable gap, and (3) the maximum current density achievable through the CNT network upon metal line fracture and at*

*the maximum bridgeable gap.* The tolerable level of cell performance degradation by the increase in series resistance (i.e., by the metal line fracture) would translate to the maximum allowable line resistance of CNT network and therefore the required CNT loading to maintain the cell performance.

### 3.3 Cell Integration and Performance Characterization

As the ultimate test of our materials engineering effort, we integrated the CNT-Ag MMCs onto commercial MJ cells and characterized the cell performance before and after fractures form under mechanical stress.

Figure 8 shows our MMC integration process flow. After the Ag seed layer deposition over a mask, the 1<sup>st</sup> Ag layer is electroplated, using a cyanide-free, AgNO<sub>3</sub>-based plating solution (E-Brite 50/50 RTP plating solution and E-Brite 50/51 replenisher). Then, the entire cell is spray-coated with an aqueous CNT solution ( $\geq 1$  g/L). The cells are placed on a moving stage ( $\leq 3.57$  mm/s) and sprayed multiple times in a repeat cycle. The solvent evaporates quickly from the heated substrate ( $\leq 150^\circ\text{C}$ ), leaving behind functionalized MW-CNTs. By controlling the CNT solution concentration, the moving speed of the sample stage under the spray nozzle and the substrate temperature, we can deposit thin, uniform layers of CNTs across the entire surface of the cell. Under the operating condition that provides fine control on CNT surface coverage, fifteen repeats result in  $>90\%$  surface coverage of CNTs on Ag. This throughput can improve with proper CNT solution concentration, stage moving speed, and stage temperature. After CNT deposition,

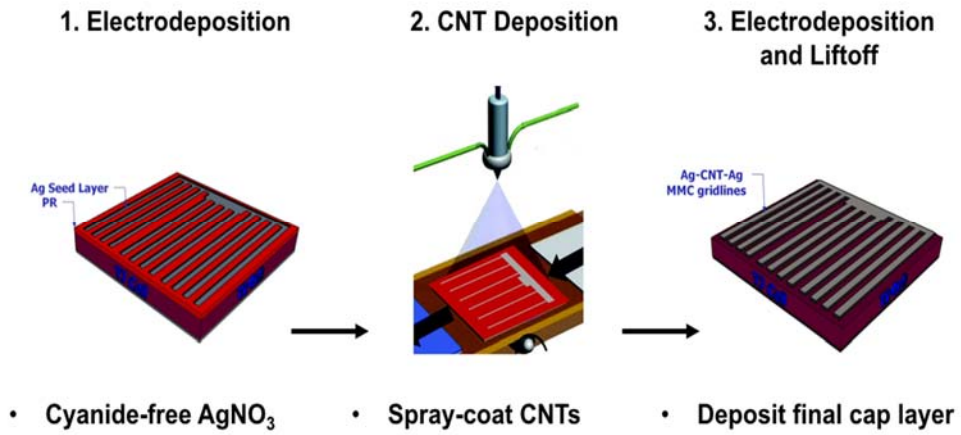


**Figure 8:** Process flow for MMC integration onto commercial TJ cells.

the cells are transferred back into the electrolytic solution for the final deposition of Ag. The second Ag layer is electroplated, resulting in a  $\sim 2$ - $\mu\text{m}$ -thick layer. Samples are then rinsed with water to remove residual plating solution and soaked in acetone to remove the photoresist and CNTs on its top by liftoff. This liftoff process defines the gridlines.

## 4 RESULTS AND DISCUSSION

This section summarizes the results from the device characterization of composite-enhanced multijunction cells in comparison to standard metallization multijunction cells. We also describe the initial results from device and composite modeling.

### 4.1 Cell Performance Characterization and Modeling

The cell performance was measured before and after introducing the cracks by conducting light and dark current-voltage sweeps (*LIV* and *DIV*) and measuring electroluminescence (EL) from the top subcell. We compared the performance of MMC-integrated (composite-enhanced) cells with that of standard-metallization cells, as a function of MMC microstructure and integration approach. The IV sweeps provide short circuit current ( $J_{sc}$ ), open circuit voltage ( $V_{oc}$ ), fill factor ( $FF$ ), efficiency ( $\eta$ ), and ideality factor ( $n$ ). One could also extract from the IV curves shunt resistance ( $R_{sh}$ ), series resistance ( $R_s$ ), and level of carrier recombinations. The EL technique visually identifies the regions of the cell that no longer generate power as well as the level of radiative recombination sites around microcracks that lead to the decrease in  $V_{oc}$ .

Figure 9 demonstrates our current capability of measuring cell performance and the data that strongly support the potential of MMCs to improve the reliability and lifetime of space solar cells. Commercial TJ cells with standard 100% evaporated Ag metallization (Control Sample) led to 53% loss in  $J_{sc}$ , while showing 29% and 68% decrease in  $FF$  and  $\eta$ .

In contrast, MMC-integrated (composite-enhanced) cells, which are identical to the standard cells other than metallization, minimized the degradation in cell performance.<sup>15,16</sup> Upon mechanically induced cell fracture, *the MMC-integrated commercial TJ cells showed no decrease in short circuit current ( $J_{sc}$ )*, while showing 26% and 35% decrease in fill factor and efficiency

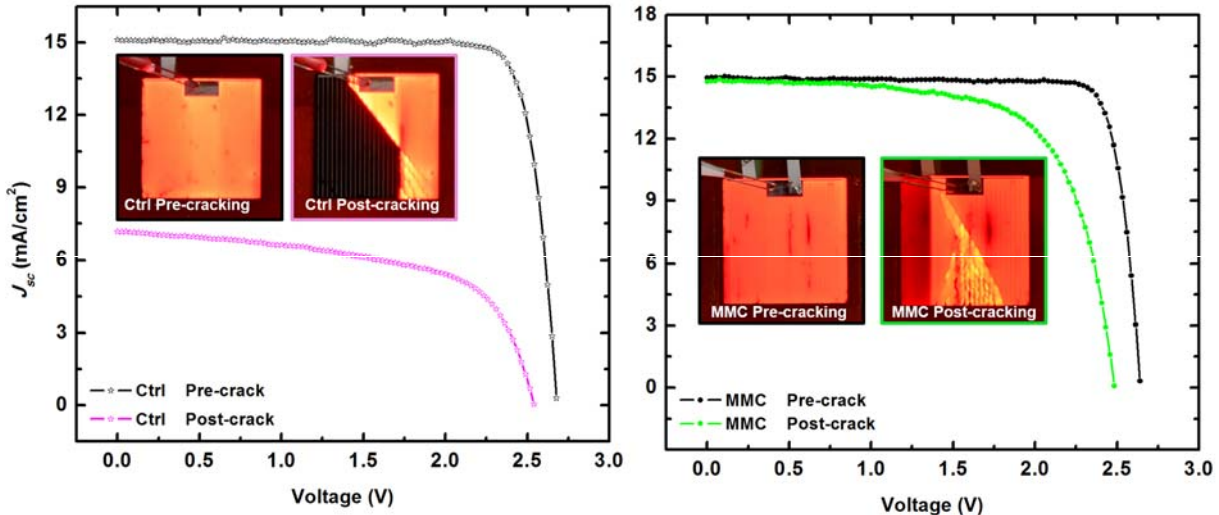


**Figure 9:** LIV and EL measurements on control sample (left) with 100% Ag gridlines, and test sample (right) with MMC gridlines.

Approved for public release; distribution is unlimited.

( $FF$  and  $\eta$ ), respectively. This result is representative of numerous standard control and MMC-integrated samples we analyzed.

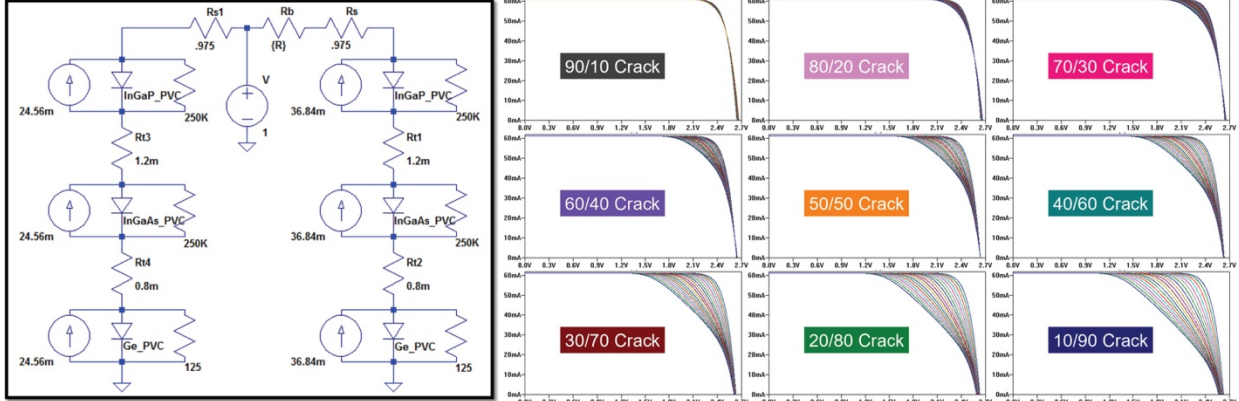


**Figure 10:** SPICE modeling of cracked TJ cells and their simulated IV curves with varying series resistance.

Simulation Program with Integrated Circuit Emphasis (SPICE) modeling was developed to simulate the IV characteristics and extract cell performance parameters, such as shunt and series resistance ( $R_{sh}$  and  $R_s$ ). The series resistance, in particular, would help determine the required amount of CNTs to be incorporated into metal to limit the performance degradation to a tolerable level (>90 % of the original performance before the cracks form). Figure 10 describes our preliminary SPICE model. We assume that the TJ cell is fractured transverse to the gridlines into effectively two sections with varying percentages (90/10 split to 10/90 split). While many more fractures occur in real life, we are partitioning the sections that are electrically connected to the busbar through metal (the 1<sup>st</sup> percentage section) and the sections that are electrically connected to the 1<sup>st</sup> percentage section through CNTs. Thus, only the 2<sup>nd</sup> fractured section has an additional series resistance ( $R_b$ ) term that represents the line resistance through the network of CNTs that bridge the gap (see the circuit diagram in Figure 10). Each simulated IV graph has multiple curves, depending on  $R_b$  that ranges from 1 to 20  $\Omega$ . While the model is a simplified view, it provides a quantitative guidance on  $R_b$ , and therefore the amount of CNTs required to maintain the cell performance.

## 4.2 Circuit Modeling to Extract Cell Parameters

We measured current-voltage (IV) characteristics of SolAero's ZTJ triple-junction PV cells reinforced with MMCs before and after substrate fracture. The cells were mechanically strained over a cylinder to introduce cracking. The IV measurements were made under a solar simulator for *LIV* curve and under complete darkness for *DIV* curve. These measurements, to which circuit models are fit, can provide key device parameters (e.g., ideality factor, saturation current, short circuit current, series resistance, and shunt resistance) as a measure of cell performance.

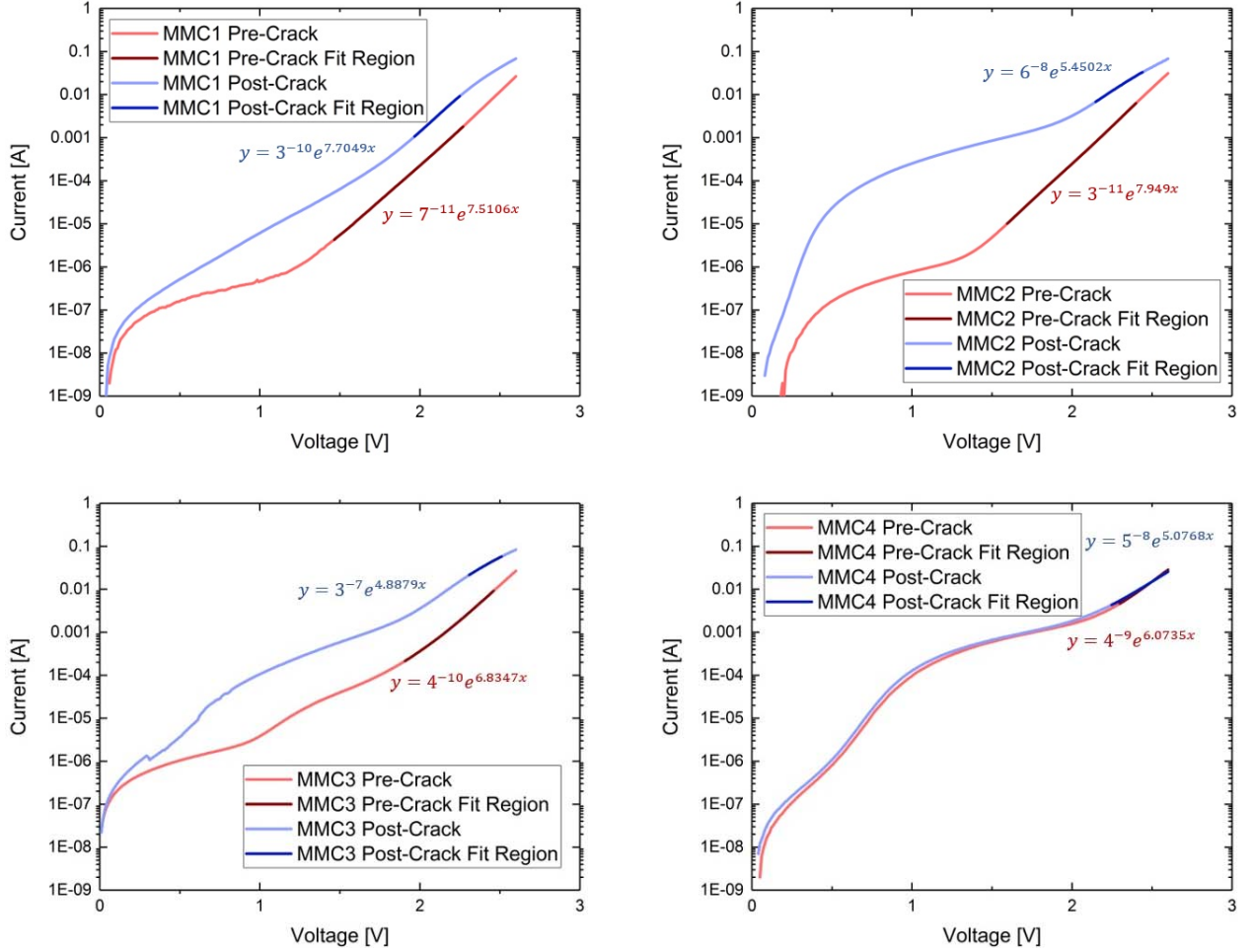


**Figure 11:** *DIV* curves of SolAero’s ZTJ triple-junction PV cells reinforced with MMCs before and after the substrate fracture.

Figure 11 shows experimentally measured *DIV* curves before (red) and after (blue) substrate fracture. For simplicity, the following *DIV* equation for a single-diode model is fit to these curves to obtain saturation current ( $I_o$ ) and ideality factor ( $n$ ).

$$I_D = I_0 \left[ \exp \left( \frac{qV}{nkT} \right) - 1 \right], \quad (1)$$

where  $I_D$ ,  $q$ ,  $V$ ,  $k$ , and  $T$  denote dark current, unit charge, potential, Boltzmann constant, and temperature, respectively. We focus on the linear region near 1.5 to 2.5 V to fit this single-diode model. For improved fit over a wider range, one could use a two-diode model, where the model could also describe the second linear region near 0.5 to 1.2 V. We note that the number of diodes used in the model has no connection to the number of subcells in the multijunction cell.

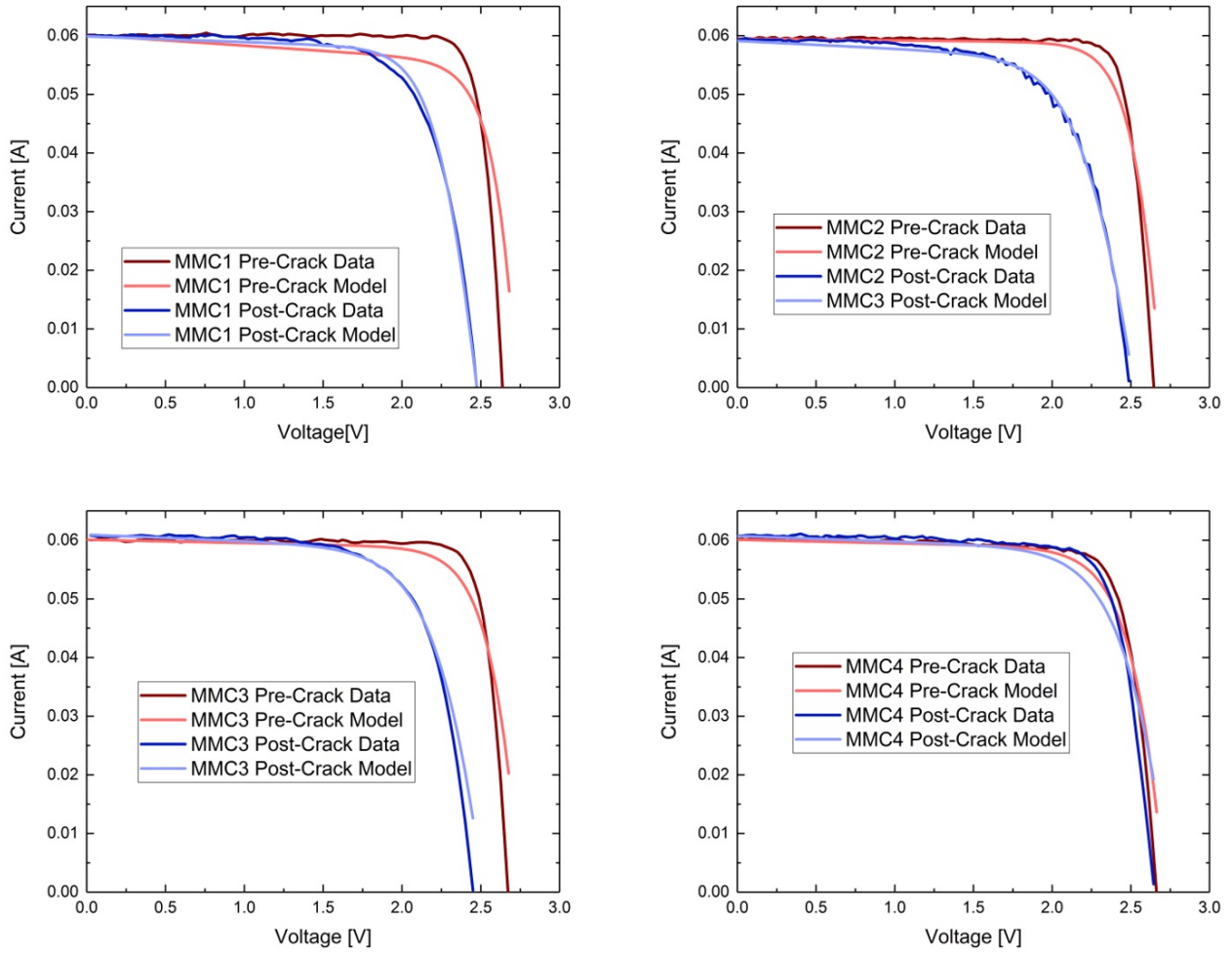


**Figure 12:** *LIV* curves of SolAero’s ZTJ triple-junction PV cells reinforced with MMCs before and after the substrate fracture.

After extracting  $I_0$  and  $n$  from the *DIV* curves, the *LIV* curves (Figure 12) can be used to obtain short circuit current ( $I_{sc}$ ), series resistance ( $R_s$ ), and shunt resistance ( $R_{sh}$ ). The short circuit current can be taken directly from the *LIV* curve at the value where voltage is equal to zero (i.e., y-intercept). The two resistance terms are extracted with a non-linear, least-squares fit in MATLAB with the following equation:

$$I = I_{sc} - I_0 \left[ \exp \left( \frac{V+IR_s}{nkT} \right) - 1 \right] - \frac{V+IR_s}{R_{sh}}, \quad (2)$$

where  $I$  is an implicit function. Table 2 below shows a summary of the extracted model parameters before and after fracturing four MMC-enhanced ZTJ triple junction PV cells.

**Table 2:** Device performance parameters extracted from model fit to experimental *DIV* and *LIV* curves.

	Control	MMC1		MMC2		MMC3		MMC4	
		Pre-crack	Post-crack	Pre-crack	Post-crack	Pre-crack	Post-crack	Pre-crack	Post-crack
$n$	4.43	5.14	5.01	4.86	7.08	5.65	7.90	6.36	7.61
$I_0$ [A]	2.4E-12	7E-11	3E-10	3E-11	6E-8	4E-10	3E-7	4E-9	5E-8
$I_{sc}$ [mA]	61.4	60.1	60.0	59.5	59.3	60.1	61.1	60.1	60.8
$R_s$ [ $\Omega$ ]	0.0023	0.00036	4.026	0.793	2.553	0.647	1.357	0.694	1.554
$R_{sh}$ [ $k\Omega$ ]	25.9	2.66	0.741	3.44	0.752	1.81	0.928	1.68	1.07

When the single-diode model is fit to the multijunction cell, the ideality factor deviates from 1 to 2 that are typical of a single junction cell. Upon fracture, the ideality factor increases in general, indicating performance degradation. The most important outcome of fracture-testing MMC-enhanced cells, however, is that  $I_{sc}$  does *not* change significantly upon cell fracture. Considering that PV cells are connected in series on a module, maintaining  $I_{sc}$  has significant implications in module reliability against substrate fracture. The cell fracture also leads to an increase in  $R_s$  and a decrease in  $R_{sh}$ , which is indicative of performance degradation. While MMC-enhanced cells showed moderate decrease in cell performance, the control cells with standard metallization showed >50% loss in  $I_{sc}$  and noticeable performance degradation (i.e., 29% and 68% decrease in  $FF$  and  $\eta$ ), where no linear regions exist in *DIV* curves, and the model can no longer be fit to the experimental data.

### 4.3 Composite Modeling to Predict Mechanical Properties

Finite element method (FEM) software, ABAQUS, was used to model how the CNT loading fraction within the silver matrix affects the overall composite mechanical properties. The modeled sandwich structure is shown in Figure 13 as a Ag/CNT/Ag, layer-by-layer stack. Since the CNT layer is a network of inter-tangled CNTs and not a solid film, the top silver layer intercalates through the voids that exist in the CNT layer and connects with the bottom silver layer. This concept is described by a simplified model, where the silver intercalates periodically in perfect circles as shown in the figure. This assumption reduces the FEM meshing by symmetry; a unit cell can represent the entire composite.

The material properties of each component in the composite are needed as an input to the model. The difficulty is that materials properties of electroplated silver are very different from what is considered as precious-metal-grade silver. The CNT network intercalated by silver would also possess material properties that are very different from those of individual MW-CNTs.

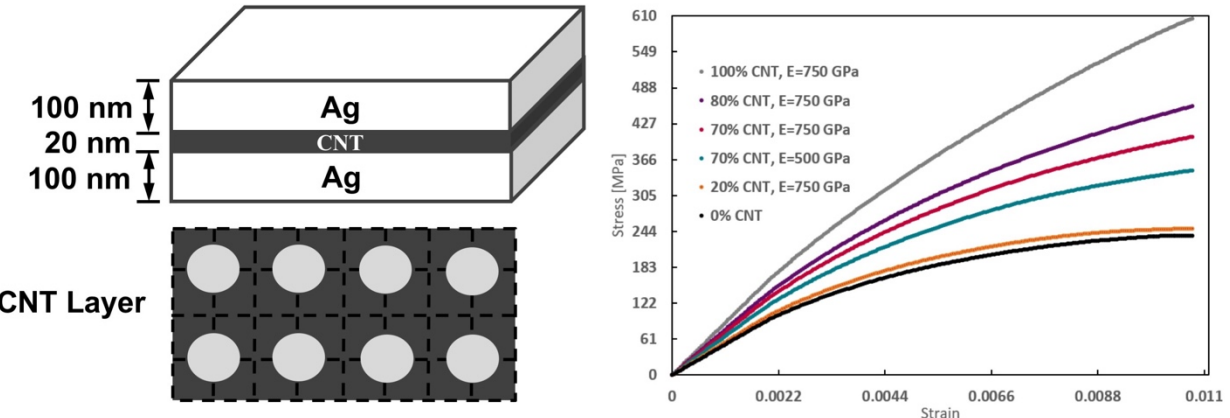


**Figure 13:** MMC composite microstructure modeled by a layer-by-layer construct of Ag/CNT/Ag stack.

To circumvent the difficulty of assigning component properties, the input mechanical properties of silver were extracted by fitting a model that allows plastic deformation (Figure 14) to experimental stress-strain data obtained from evaporated 4- $\mu\text{m}$ -thick 100% Ag. The stress-strain DMA data were provided by the Landi group at Rochester Institute of Technology (RIT).

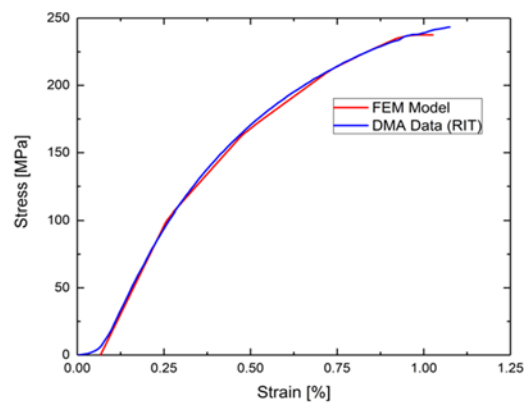
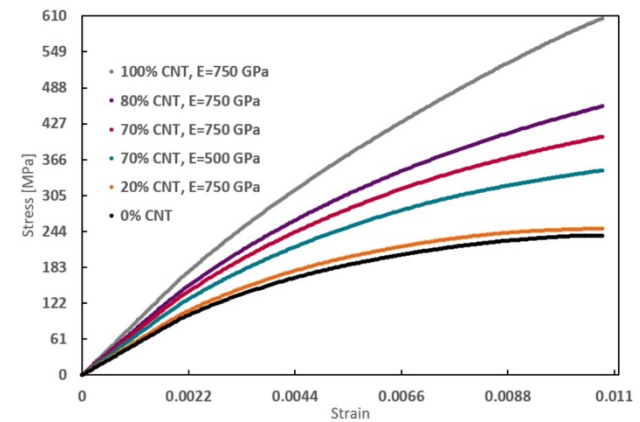


**Figure 14:** Experimental and model stress-strain curves of Ag deposited by evaporation.

in Figure 13, and a summary of MMC modulus, extracted from the initial linear region of each curve, is given in Table 3.



For ease of fitting the model, we arbitrarily introduced 13 points at which plastic deformation is allowed. One could potentially introduce more points to smooth out the fitting. The model fit in Figure 14 gave an elastic modulus of evaporated silver films to be 47.1 GPa along with the plastic deformation trends. To model 100% silver, the surface coverage of CNTs in the interlayer shown in Figure 13 was assumed to be zero.

For effective material properties of the CNT-silver interlayer, we assigned a large elastic modulus of 750 GPa as an initial estimate; this effective modulus can be used as a variable parameter to fit the experimental data in the future. The stress-strain curves of MMCs with different CNT loading are shown

**Table 3:** Summary of MMC modulus as a function of CNT loading.

<b>CNT %</b> <b>(<math>E_{CNT} = 750\text{GPa}</math>)</b>	<b>MMC Modulus (GPa)</b>
0	47.030
20	50.499
70	65.479
80	69.916
100	80.596

## 5 CONCLUSIONS

During the entire project period (2014-2017), we have fully integrated our MMCs onto commercial multijunction cells and demonstrated that MMC gridlines provide strongly pronounced crack-tolerance, compared to standard-metallization multijunction cells. Upon introducing cracks to the cells, samples with the MMC gridlines exhibit virtually zero loss in  $J_{sc}$ , while retaining a continuous electroluminescence glow. The latter is strong evidence that the fractured portion of the substrate is electrically connected. In contrast, fractured control cells show a significant loss in  $J_{sc}$  up to 54% with noticeably dark regions during EL measurements. In addition, the average loss in  $FF$  and  $\eta$  in control cells is 32% and 54%, respectively, compared to 16% and 19% for MMC-enhanced cells. This demonstration supports that our MMC gridlines are suitable to replace traditional gridlines and to help mitigate the loss in cell performance as microcracks develop in cells.

While we have demonstrated the technological advantages of MMCs to increase the reliability and lifetime of space solar photovoltaics, we began to understand how CNT incorporation into electroplated silver affects device parameters and mechanical properties. Using a single-diode model, we began to extract device parameters, such as  $I_0$ ,  $n$ ,  $I_{sc}$ ,  $R_s$ , and  $R_{sh}$  before and after substrate fracture. We also began to model the mechanical properties of MMCs, using a final element method where the material properties of each component (i.e., silver and an effective interlayer that consists of a contiguous sheet of CNTs with periodically open circular holes through which silver intercalates) are used as an input. These modeling capabilities would allow us to compare in a quantitative manner MMC-enhanced cells against the cells with conventional metallization for our future work.

From the manufacturing stand point, we make use of low-cost, multiwalled CNTs embedded in Ag matrix to mechanically and electrically reinforce metal gridlines. These composite metal gridlines show strong potential to replace conventional ones deposited by evaporation. Our metal matrix composites (MMCs) assume a layer-by-layer microstructure that consists of Ag/CNT/Ag, and we achieve this architecture, using simple deposition methods. Our process relies on electrochemical deposition (plating) of Ag, a low-cost, highly reproducible alternative to vacuum metal deposition. We also use spray-coating as a fast, cost-effective, and easily scalable method of depositing CNTs. The combined use of plating and spray-coating provides a manufacturable path to integrate MMCs. In 2017, we have established our partnership with SolAero and formed a new company Osazda Energy, LLC to commercialize the MMC technology. Osazda is now simultaneously working on developing CNT-incorporated Ag paste (widely used on terrestrial solar cells) and the paste application (i.e., adhesion layer formation and furnace firing schedule) on Si substrates to broadly translate the MMC technology to a much bigger terrestrial market.

## REFERENCES

- 1 M. Stan, D. Aiken, B. Cho, A. Cornfeld, J. Diaz, V. Ley, A. Korostyshevsky, P. Patel, P. Sharps, and T. Varghese, "Very high efficiency triple junction solar cells grown by MOVPE," *Journal of Crystal Growth* **310**, 2008, pp. 5204-5208.
- 2 C. Fetzer, B. Jun, K. Edmondson, S. Khemthong, K. Rouhani, R. Cravens, R. Bardfield, and M. Gillanders, "Production Ready 30% Efficient Triple Junction Space Solar Cells," in *PVSC: 2008 33rd IEEE Photovoltaic Specialists Conference, Vols 1-4*, San Diego, CA, pp. 93-96.
- 3 T. Takamoto, M. Yamaguchi, S. J. Taylor, E. Ikeda, T. Agui, and H. Kurita, "High-efficiency radiation-resistant InGaP/GaAs tandem solar cells," in *Conference Record of the Twenty Sixth Ieee Photovoltaic Specialists Conference - 1997* Anaheim CA, 1997, pp. 887-890.
- 4 D. C. Law, J. C. Boisvert, E. M. Rehder, P. T. Chiu, S. Mesropian, R. L. Woo, X. Q. Liu, W. D. Hong, C. M. Fetzer, S. B. Singer, D. M. Bhusari, K. M. Edmondson, A. Zakaria, B. Jun, D. D. Krut, R. R. King, S. K. Sharma, and N. H. Karam, "Recent Progress of Spectrolab High-Efficiency Space Solar Cells," in *Nanophotonics and Macrophotronics for Space Environments for Space Environments Conference*, San Diego, CA, 2013.
- 5 B. Jun, C. M. Fetzer, K. Rouhani, W. G. Wise, D. Krut, K. Bui, D. Hom, C. J. Cho, J. Z. Wu, R. Anaya, R. Bardfield, D. A. Russell, P. Leung, M. Gillanders, S. K. Sharma, and J. P. Hanley, "Final Qualification Test Results of X TJ Triple Junction Space Solar Cell to AIAA - S-111-2005 and Spectrolab Test Standards," in *35th IEEE Photovoltaic Specialists Conference*, Honolulu, HI, 2010.
- 6 N. H. Karam, R. R. King, B. T. Cavicchi, D. D. Krut, J. H. Ermer, M. Haddad, L. Cai, D. E. Joslin, M. Takahashi, J. W. Eldredge, W. T. Nishikawa, D. R. Lillington, B. M. Keyes, and R. K. Ahrenkiel, "Development and characterization of high-efficiency Ga0.5In0.5P/GaAs/Ge dual- and triple-junction solar cells," *IEEE Transactions on Electron Devices* **46**, 1999, pp. 2116-2125.
- 7 G. Strobl, R. Dietrich, J. Hilgarth, W. Kostler, R. Kern, M. Nell, S. Rothenbacher, A. W. Bett, F. Dimroth, M. Meusel, R. Campesato, C. Flores, G. Timo, G. Smekens, J. Vanbegin, G. Raskin, W. Geens, G. LaRoche, G. Hey, C. Signorini, and S. Taylor, "Advanced GaInP/Ga(In)As/Ge triple junction space solar cells," *Proceedings of 3rd World Conference on Photovoltaic Energy Conversion*, Osaka, Japan, 2003, pp. 658-661.
- 8 M. Stan, D. Aiken, B. Cho, A. Cornfeld, J. Diaz, A. Korostyshevsky, V. Ley, P. Patel, P. Sharps, and T. Varghese, "Evolution Of The High Efficiency Triple Junction Solar Cell

Approved for public release; distribution is unlimited.

for Space Power," in *PVSC: 33rd IEEE Photovoltaic Specialists Conference, Vols 1-4* San Diego, CA, 2008, pp. 1450-1455.

9 G. Timo, C. Flores, and R. Campesato, "Bottom cell growth aspects for triple junction InGaP/(In)GaAs/Ge solar cells," *Crystal Research and Technology* **40**, 2005, pp. 1043-1047.

10 M. W. Wanlass, P. Ahrenkiel, D. S. Albin, J. J. Carapella, A. Duda, K. Emery, D. J. Friedman, J. Geisz, K. Jones, A. Kibbler, J. Kiehl, S. Kurtz, W. E. McMahon, T. Moriarty, J. M. Olson, and A. J. Ptak," Proceedings of the Fourth World Conference on Photovoltaic Energy Conversion, Waikoloa, HI, 2006, p. 729.

11 M. W. Wanlass, S. P. Ahrenkiel, R. K. Ahrenkiel, D. S. Albin, J. J. Carapella, A. Duda, J. F. Geisz, S. Kurtz, T. Moriarty, R. J. Wehrer, and B. Wersman," *Proceedings of the 31st IEEE Photovoltaic Specialists Conference*, Orlando, FL, 2005, p. 530.

12 J. F. Geisz, D. J. Friedman, J. S. Ward, A. Duda, W. J. Olavarria, T. E. Moriarty, J. T. Kiehl, M. J. Romero, A. G. Norman, and K. M. Jones, "40.8% efficient inverted triple-junction solar cell with two independently metamorphic junctions," *Appl. Phys. Lett.* **93**, 2008, p. 123505.

13 J. F. Geisz, S. Kurtz, M. W. Wanlass, J. S. Ward, A. Duda, D. J. Friedman, J. M. Olson, W. E. McMahon, T. E. Moriarty, and J. T. Kiehl, "High-efficiency GaInP/GaAs/InGaAs triple-junction solar cells grown inverted with a metamorphic bottom junction," *Appl. Phys. Lett.* **91**, 2007, p. 023502.

14 National Renewable Energy Laboratory, "High-Concentration III-V Multijunction Solar Cells," 2017, <<http://www.nrel.gov/pv/high-concentration-iii-v-multijunction-solar-cells.html>>.

15 O. K. Abudayyeh, G. K. Bradshaw, S. Whipple, D. M. Wilt, Nathan Gap, Cayla Nelson, Nathanael Cox, Aaron Rape, Brian Landi, and Sang Han "Metal Matrix Composite Solar Cell Metallization," European Space Power Conference, Thessaloniki, Greece, 16 03001, 2017, <https://doi.org/10.1051/e3sconf/20171603001>.

16 O. K. Abudayyeh, N. D. Gapp, C. Nelson, D. M. Wilt, and S. M. Han, "Silver-Carbon-Nanotube Metal Matrix Composites for Metal Contacts on Space Photovoltaics," *IEEE J. Photovolt.* **6**, 2016, pp. 337-342.

17 M. M. J. Treacy, T. W. Ebbesen, and J. M. Gibson, "Exceptionally high Young's modulus observed for individual carbon nanotubes," *Nature* **381**, 1996, pp. 678-680.

18 P. Poncharal, Z. L. Wang, D. Ugarte, and W. A. de Heer, "Electrostatic Deflections and Electromechanical Resonances of Carbon Nanotubes," *Science* **283**, 1999, pp. 1513-1516.

19 P. G. Collins, M. Hersam, M. Arnold, R. Martel, and P. Avouris, "Current Saturation and Electrical Breakdown in Multiwalled Carbon Nanotubes," *Phys. Rev. Lett.* **86**, 2001, pp. 3128-3131.

20 H. Dai, E. W. Wong, and C. M. Lieber, "Probing Electrical Transport in Nanomaterials: Conductivity of Individual Carbon Nanotubes," *Science* **272**, 1996, pp. 523-526.

21 S. Frank, P. Poncharal, Z. L. Wang, and W. A. de Heer, "Carbon Nanotube Quantum Resistors," *Science* **280**, 1998, pp. 1744-1746.

22 Cheap Tubes, Inc., 2017,  
<https://www.cheaptubes.com/?gclid=CKDAxOnx6tECFYGAfgodSfYBVw>.

23 S. R. Bakshi, D. Lahiri, and A. Agarwal, "Carbon nanotube reinforced metal matrix composites - a review," *Int. Mater. Rev.* **55**, 2010, pp. 41-64.

24 J. T. H. Tsai and H.-L. Hwang, "Carbon Nanotube Reinforced Conductors for Flexible Electronics," *Journal of Display Technology* **5**, 2009, pp. 232-235 .

25 Q. Chen, "Carbon Nanotube Reinforced Metal Composites," Patent No. 7,651,766 B2 11/437,180 (2010).

26 Q. Chen, "Electrochemical Codeposition Methods for Forming Carbon Nanotube Reinforced Metal Composites," Patent No. 2010/0122910 A1 12/693,240 (2010).

27 N. Ferrer-Anglada, V. Gomis, Z. El-Hachemi, U. D. Weglikovska, and S. Roth, "Carbon nanotube based composites for electronic application: CNT-conducting polymers, CNT-Cu," *Phys. Stat. Sol. (a)* **203**, 2006, pp. 1082-1087.

28 C. Guo, Y. Zuo, X. Zhao, J. Zhao, and J. Xiong, "The effects of pulse-reverse parameters on the properties of Ni-carbon nanotubes composite coatings," *Surf. Coat. Technol.* **201**, 2007, pp. 9491-9496 .

29 Y.-H. Li, W. Housten, Y. Zhao, and Y. Q. Zhu, "Cu/single-walled carbon nanotube laminate composites fabricated by cold rolling and annealing," *Nanotechnology* **18**, 2007, p. 205607.

30 S. Zhang, D. Sun, Y. Fu, and H. Du, "Toughening of hard nanostructural thin films: a critical review," *Surf. Coat. Technol.* **198**, 2005, pp. 2-8.

31 N. D. Cox, A. Rape, M. Pham, J. E. Rossi, A. R. Bucossi, and B. J. Landi, "Free-standing silver/carbon nanotube metal matrix composite thin films," *Journal of Materials Science* **51**, 2016, pp. 10935-10942.

32 S. J. Yoo, S. H. Han, and W. J. Kim, "A combination of ball milling and high-ratio differential speed rolling for synthesizing carbon nanotube/copper composites," *Carbon* **61**, 2013, pp. 487-500.

33 A. Lorenz, A. Kraft, C. Gredy, A. Filipovic, S. Binder, K. Kruger, J. Bartsch, F. Clement, D. Biro, R. Preu, and H. Reinecke, "Comprehensive Comparison of Different Fine Line Printing Technologies Addressing the Seed and Plate Approach with Ni-Cu-Plating," (2015), <<https://www.researchgate.net/publication/294877982>>.

34 F. Valentini, A. Amine, S. Orlanducci, M. L. Terranova, and G. Palleschi, "Carbon Nanotube Purification: Preparation and Characterization of Carbon Nanotube Paste Electrodes," *Anal. Chem.* **75**, 2003, pp. 5413-5421.

35 X. Tan, M. Li, P. Cai, L. Luo, and X. Zou, "An amperometric cholesterol biosensor based on multiwalled carbon nanotubes and organically modified sol-gel/chitosan hybrid composite film," *Anal. Biochem.* **337**, 2005, 111-120.

36 T. Ramanathan, F. T. Fisher, R. S. Ruoff, and L. C. Brinson, "Amino-Functionalized Carbon Nanotubes for Binding Polymers and Biological Systems," *Chem. Mater.* **17**, 2005, pp. 1290-1295.

37 Wikipedia, <<http://en.wikipedia.org/wiki/Carboxyl>>, "Carboxylic acid."

38 Wikipedia, <<http://en.wikipedia.org/wiki/Amine>>, "Amine."

39 O. Abudayyeh, N. D. Gapp, D. M. Wilt, and S. M. Han, "Methods to Mitigate Stress-Induced Metal Line Fractures for Thin-Film Solar Cells, Using Metal-Carbon-Nanotube Composites," Patent No. Application No. PCT/US2016/038197 (2016).

40 "Frequently Asked Questions: Dynamic Mechanical Analysis (DMA)," PerkinElmer (Copyright 2008-2013), <[https://www.perkinelmer.com/CMSResources/Images/44-74546GDE\\_IntroductionToDMA.pdf](https://www.perkinelmer.com/CMSResources/Images/44-74546GDE_IntroductionToDMA.pdf)>.

## LIST OF ACRONYMS, ABBREVIATIONS, AND SYMBOLS

Acronym/ Abbreviation	Description
AM0	Air Mass
CNT	Carbon Nanotubes
DIV	Dark Current-Voltage
DMA	Dynamic Mechanical Analysis
EL	Electroluminescence
FEM	Finite Element Method
IMM	Inverted Metamorphic Multijunction
LIV	Light Current-Voltage
LLC	Limited Liability Company
MJ	Multijunction
MW	Multi-Walled
MAVEN	Mars Atmosphere and Volatile Evolution Mission
MMC	Metal matrix composite
NASA	National Aeronautics and Space Administration
PV	Photovoltaic
RACK	Across Cleaves and cracKs
RIT	Rochester Institute of Technology
SEM	Scanning Electron Microscope
SPICE	Simulation Program with Integrated Circuit Emphasis
SW	Single-Walled
TJ	Triple Junction

Symbol	Description
$V_{oc}$	Open circuit voltage
$J_{sc}$	Short circuit current
$FF$	Fill factor
$\eta$	Efficiency
$n$	Ideality factor
$R_{sh}$	Shunt resistance
$R_s$	Series resistance
$R_b$	Additional series resistance in the cracks
$I_D$	Diode current
$q$	Unit charge
$V$	Voltage
$k$	Boltzmann constant
$T$	Temperature

Approved for public release; distribution is unlimited.

## DISTRIBUTION LIST

DTIC/OCP  
8725 John J. Kingman Rd, Suite 0944  
Ft Belvoir, VA 22060-6218

1 cy

AFRL/RVIL  
Kirtland AFB, NM 87117-5776

1 cy

Official Record Copy  
AFRL/RVSV/David Wilt

1 cy

Approved for public release; distribution is unlimited.